Passive Sensor Evaluation for Unmanned Ground Vehicle Mud Detection

A. L. Rankin and L. H. Matthies
Jet Propulsion Laboratory, California Institute of Technology, 4800 Oak Grove Drive, Pasadena, California 91109

Received 10 September 2009; accepted 13 March 2010

Detecting mud hazards is a significant challenge to unmanned ground vehicle (UGV) autonomous off-road navigation. A military UGV stuck in a body of mud during a mission may need to be sacrificed or rescued, both unattractive options. The Jet Propulsion Laboratory is currently developing a daytime mud detection capability under the U.S. Army Research Laboratory Robotics Collaborative Technology Alliances program using UGV-mounted sensors. To perform robust mud detection under all conditions, we expect that multiple sensors will be necessary. A passive mud detection solution is desirable to meet future combat system requirements. To characterize the advantages and disadvantages of candidate passive sensors, outdoor data collections have been performed on wet and dry soil using visible, multispectral (including near-infrared), shortwave infrared, midwave infrared, long-wave infrared, polarization, and stereo sensors. In this paper, we examine the cues for mud detection that each of these sensors provide, along with their deficiencies, and we illustrate localizing detected mud in a world model that can used by a UGV to plan safe paths. We mostly limit our examination to mud detection during the daytime under ideal conditions: isolated wet soil surrounded by dry soil during nominal weather, i.e., no precipitation, calm wind, and near-average temperatures. © 2010 Wiley Periodicals, Inc.

1. INTRODUCTION

There are many types of terrain that an unmanned ground vehicle (UGV) can encounter during autonomous navigation. Some of the terrain types are pavement, gravel, soil of varying firmness, mud, snow, ice, water, and vegetation of various heights and thicknesses. The ability to detect and avoid hazardous terrain poses a current challenge to the acceptance and proliferation of tactical UGVs (Mills, 2007). Because water and mud are prevalent in many regions during a portion of the year, robust detection of these hazards is a critical perception requirement for UGV autonomous navigation.

Bodies of water and mud need to be detected at a sufficient distance (which is a function of the UGV's current speed) to allow the UGV to evade them. A UGV that becomes stuck in water or mud during an autonomous military mission may require rescue, potentially drawing critical resources away from the primary mission and soldiers into harm's way. Alternatively, a UGV stuck in water or mud during an autonomous military mission may need to be sacrificed, an expensive proposition. Under the U.S. Army Research Laboratory (ARL) Robotics Collaborative Technology Alliances (RCTA) program, the Jet Propulsion Laboratory (JPL) was tasked with developing a water and mud detection capability for UGVs. In previous papers, we have reported our progress on detecting and localizing bodies of water in a world model used to plan safe paths (Matthies, Bellutta, & McHenry, 2003; Rankin & Matthies, 2006; Rankin, Matthies, & Huertas, 2004). In this paper, we report our progress on evaluating sensors applicable to mud detection from a UGV.

Although mud detection for UGV autonomous navigation is a relatively new research area, techniques to estimate soil moisture content (SMC) have been studied for decades for agricultural applications (Hamrita, Tollner, & Schafer, 2000). SMC has been estimated using devices requiring contact with the ground and via remote sensing (Sudduth, Hummel, & Birrell, 1997; Whalley & Stafford, 1992). Remote sensing of soil moisture has been performed with sensors mounted to satellites, aerial vehicles, and ground vehicles. Satellite methods of soil moisture estimation use thermal infrared (Wetzel, Atlas, & Woodward, 1984), passive and active microwave (Dubois & van Zyl Engman, 1995; Wigneron, Schmugge, Chanzy, & Kerr, 1998), and multispectral (Zeng, Feng, & Xiang, 2004) sensors. The satellite methods are useful in characterizing the SMC of large fields but lack the resolution necessary for detecting small but severe UGV mud hazards. Aerial methods of soil moisture estimation use passive and active microwave sensors (Archer, Shutko, Coleman, Haldin, Novichikhin, et al., 2004; O'Neill, Chauhan, & Jackson, 1996). Unmanned aerial vehicles (UAVs) with microwave sensors have been used to estimate soil moisture through vegetation clutter (such as a corn field). However, they also lack the resolution for detecting small but severe UGV mud hazards.

Ground vehicle methods of soil moisture estimation have also used passive microwave sensors (Archer, Shutko, Coleman, Haldin, Sidorov, et al., 2006). But the antennas

tend to be bulky and have been mounted directly downward, requiring a UGV to drive on potentially hazardous terrain to characterize it. Dupont, Collins, Coyle, and Roberts (2008) classified terrain types, including mud, by using proprioceptive sensors that measure UGV vibration and estimate applied wheel torques. Angelova, Matthies, Helmick, and Perona (2007) developed an algorithm to predict the amount of wheel slippage that terrain in the distance will cause using stereo vision sensors. However, these methods also require a UGV to drive on potentially hazardous terrain to characterize or learn about it.

Alshikaili (2007) used a noncontact infrared thermocouple to predict SMC based on soil temperature from a tripod. But a fieldable weather station was required to determine some model parameters (air temperature, solar radiation, relative humidity, wind speed), soil emissivity needed to be manually selected on the thermocouple, and the level of soil compaction needed to be specified. Powers and Davis (2009) have experimented with a monostatic active polarimeter designed to classify solid ground and mud for UGVs. But because there are military operations when it may be desirable for UGVs to operate without emitting strong, detectable electromagnetic signals, a passive perception solution to mud detection is also desirable.

Under the ARL Demo III, Defense Advanced Research Projects Agency (DARPA) Perception for Off-Road Robots (PerceptOR), and RCTA programs, JPL has performed daytime data collections on wet and dry soil using a variety of passive imaging sensors that spans much of the visible through thermal infrared portion of the electromagnetic spectrum. These include color, multispectral including near-infrared (NIR), short-wave infrared (SWIR), midwave infrared (MWIR), and long-wave infrared (LWIR), and polarization cameras. Table I lists the primary specifications of each camera. Some of our color and MWIR data sets include stereo imagery.

In this paper, we show sample images of mud from each camera, describe the cues for mud that each class of camera can provide, describe the limitations of each class of camera for detecting mud, illustrate some basic techniques for detecting mud and disambiguating mud from similar features, and illustrate fusing cues for mud in a terrain map using a polarization camera and a stereo pair of color cameras. We start this work focusing primarily on detecting mud where it is most likely to be encountered by a UGV: on dirt trails or in open dirt fields. We recognize that there are more difficult cases, such as detecting mud when the entire ground is wet and the surface is not soil. Difficult scenarios such as these will be addressed in future work. Here, we mostly limit our examination to mud detection during the daytime under ideal conditions: isolated wet soil surrounded by dry soil during nominal weather, i.e., no precipitation, calm wind, and near-average temperatures. Although isolated mud patches may be a minor concern for automobile-size UGVs, they can pose significant mobility challenges to smaller wheeled UGVs.

2. MUD CUES FROM COLOR

It is commonly observed that wet soil is considerably darker than dry soil in visible imagery. This is because changing the medium surrounding soil particles from air to water decreases the particle's relative refractive index, increasing the average degree of forwardness of scattering. As a result, incident photons have a higher probability of being absorbed (Twomey, Bohren, & Mergenthaler, 1986). Perrson (2005) found that soil gradually becomes darker as it is wet to a soil moisture level of 0.25 m^3m^{-3} (volume water per unit volume of soil). Beyond that level, some soils start to become lighter again as water starts becoming visible on the surface.

First, we consider the nominal case in which the mud is unsaturated and surrounded by dry soil. As illustrated in Figure 1, unsaturated mud tends to be significantly darker than surrounding dry soil, to have a hue similar to that of the surrounding dry soil, and to have a strong edge boundary. The right image in Figure 1 illustrates mud detection by performing edge detection and thresholding the average intensity difference between the interior and local exterior of closed edges. Therefore, ground regions significantly darker than surrounding terrain can be a cue for mud. But shadows are also ground regions significantly darker than surrounding terrain. To disambiguate mud from shadows, one can analyze the color content of the dark region (Ollis & Stentz, 1997). Shadows inherently do not receive direct light from the primary light source. As a result, blue light

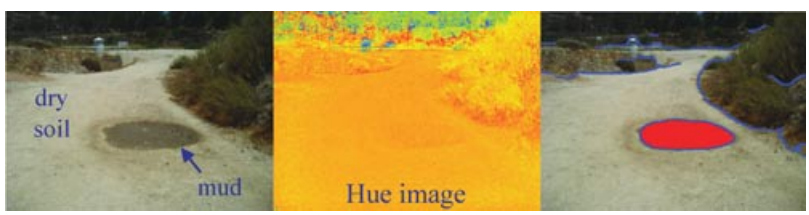

Figure 1. Color can be useful in segmenting unsaturated mud from surrounding dry soil. Unsaturated mud tends to be darker than surrounding dry soil, to have a hue similar to that of the surrounding dry soil, and to have a strong edge boundary. The right image illustrates mud detection by performing edge detection and thresholding the average intensity difference between the interior and local exterior of closed edges.

Table I. Primary specifications of the passive imaging sensors evaluated for mud detection.

Manufacturer model	Camera description	Spectral sensitivity (nm)	Camera picture	Mass w/o lens (g)	Power (W)	Dimensions (w/o lens) H × W × L (cm)	Resolution, focal length, field of view
Hitachi HV-F31	3-CCD color cameras	400–700		600	9	6.5 × 6.5 × 13.0	1,024 × 768 4 mm 55.8 × 42.7 deg
			http://www.hitachikokusai.us				
Bossa Nova Technologies SAMBA	Monochrome camera with automatic polarization switching	400–700		800	6	8.0 × 8.0 × 10.0	640 × 480 12.5 mm 29 × 22 deg
			http://www.bossanovatech.com				
Bossa Nova Technologies SALSA	Linear Stokes polarization camera	520–550		1,000	6	10.2 × 10.2 × 15.2	782 × 582 20 mm 20 × 15 deg
			http://www.bossanovatech.com				
Duncan Tech MS2100 (no longer available)	3-CCD multispectral cameras w/beam splitter	400–1,000		1,620	10	8.9 × 9.7 × 14.9	656 × 494 14 mm 25.8 × 19.5 deg
			http://www.redlake.com				
Sensors Unlimited SU320M-1.7RT	SWIR camera with InGaAs sensor	900–1,700		300	1.6	5.0 × 6.0 × 9.5	320 × 240 50 mm 14.6 × 10.9 deg
			http://www.sensorsinc.com				
Spiricon SP-1550IR (no longer available)	SWIR camera (CCD focal plane array coated with a phosphor)	1,460–1,625		98*	1.32*	3.7 × 3.4 × 5.6*	640 × 480 25 mm 14.5 × 10.8 deg
			http://www.ophir-spiricon.com, *for current model SP-1550M				
Cincinnati Electronics NC256	MWIR camera with uncooled InSb sensor	3,600–5,000		1,845.8	16	7.1 × 7.1 × 29.5	256 × 256 7 mm 67.5 × 62.4 deg
			http://www.cinele.com				
Thermoteknix Miricle 110 KB	LWIR camera with Alpha Silicon uncooled microbolometer	7,000–14,000		140	3.3	4.8 × 4.3 × 5.6	384 × 288 15 mm 48 × 37 deg
			http://www.thermoteknix.com				

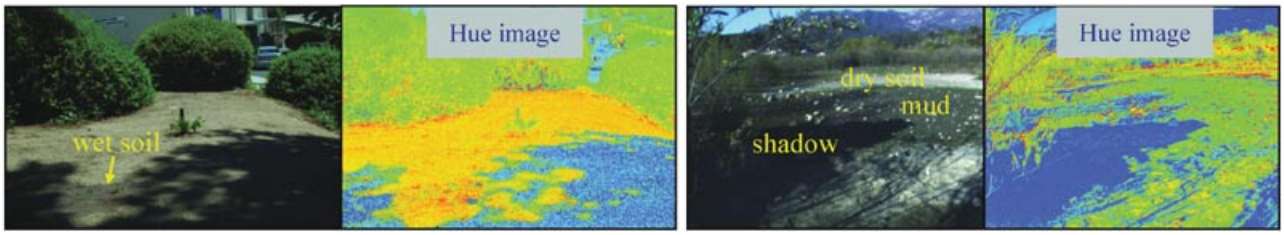

Figure 2. Two examples illustrating that soil in shadow tends to be bluer than nonshadowed wet or dry soil. But nonshadowed wet soil tends to have a hue similar to that of dry soil. The left scene was imaged a few minutes after pouring cold water on the soil. The right scene is of a drying pond in the Los Angeles County Arroyo Seco.

tends to scatter more relative to red and green light, giving shadows a higher blue saturation than neighboring regions (Wells, 2007). This is illustrated in Figure 2 for a recently wet patch of soil and for a preexisting body of mud. In both examples, the soil in shadow is bluer than nonshadowed soil.

Under off-nominal conditions, such as after precipitation when the entire ground is wet, color analysis may be useful in detecting extremely muddy terrain. Small patches of sitting water tend to form where the ground is oversaturated. These small patches of water are a cue for muddy terrain and can be detected from color analysis if the water is reflecting the sky or stereo analysis if the water is reflecting background terrain (Rankin & Matthies, 2006). Figure 3 illustrates detecting oversaturated terrain by detecting reflections of the sky.

In summary, isolated mud can be detected from color imagery by segmenting regions significantly darker than surrounding terrain (but with a hue similar to that of the surrounding terrain). Extremely muddy terrain can be detected by segmenting small water patches that reflect the sky. Color can also be useful in disambiguating nonshadowed mud from shadows. However, color is probably not very useful in determining whether the terrain in a shadow is mud or in distinguishing the muddiest portion of terrain when the entire ground is wet (except where there are small patches of water reflecting the sky).

3. MUD CUES FROM MULTISPECTRAL DATA

In the remote sensing community, it is well known that LandSat multispectral data on bare soil fall on a line (referred to as the *soil line*) when plotted in NIR vs. red reflectance space. Bare soil pixel placement on the *soil line* depends on SMC. Wet bare soil maps to one end of the line and dry bare soil maps to the opposite end. To determine whether this phenomenology is valid from a ground-based sensor, we performed data collections on wet and dry soil with a Duncan Tech MS2100 multispectral camera having spectral sensitivity from 400 to 1,000 nm. This camera is based on a color-separating prism and three imaging channels that allow simultaneous image acquisition of four spectral bands (red, green, blue, and NIR) through a common aperture.

Two data collections were performed with the multispectral camera mounted to a tripod: one in an area that contained bare soil (both in and out of shadow) and vegetation, and the second looking down a long dirt road lined with vegetation. Water was poured over a small portion of both scenes and allowed to soak into the ground. Figure 4 contains images of the red and NIR bands for the first scene. It also contains a NIR vs. red reflectance plot of the pixels in the boxes overlaid on the NIR image. The red box contains dry soil, the green box contains wet soil, and the blue box contains dry soil in shadow. The yellow line

Figure 3. When the entire ground is wet after precipitation, oversaturated mud regions can be identified by detecting reflections of the sky in small patches of standing water. From left to right are a scene from Ft. Knox, the brightness color component, the saturation color component, and sky-reflection–based water detection.

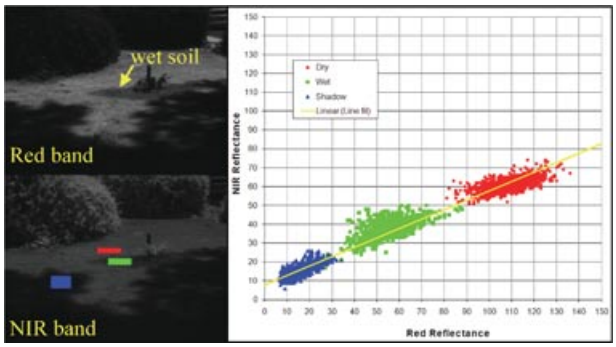

Figure 4. In NIR vs. red reflectance space, dry, wet, and shadowed soils lie on a line referred to as the *soil line* in remote sensing literature.

is a least squares line fit of the data. From this example, it appears that the *soil line* phenomenology is also valid from a ground-based sensor. Because dry soil in shadow plots to the left of wet soil on the *soil line*, it is more difficult to disambiguate shadows from wet soil than shadows from dry soil.

Figure 5 illustrates using multispectral bands to segment wet soil. Red and NIR bands [Figures 5(a) and 5(b)] can be used to generate a normalized difference vegetation index (NDVI) image [Figure 5(c)] (Zeng et al., 2004). If the slope and y intercept of the *soil line* is known, a normal distance to the soil line (DTSL) image [Figure 5(e)] and a distance along the soil line (DASL) image [Figure 5(f)] can be generated. The NDVI and normal DTSL images can be used to segment soil from vegetation [Figure 5(g)]. A brightness image [Figure 5(d)], which is derived from the visible bands, and the DASL image can be used to segment wet soil from dry soil [Figure 5(h)].

Water, snow, and ice all have larger red reflectance values than NIR, bare soil has a slightly larger NIR reflectance than red, and vegetation has a much larger NIR reflectance than red. Some typical NDVI values (from overhead sensors) are 0.7 for dense vegetation, 0–0.1 for bare soil, −0.046 for snow and ice, and −0.257 for water (Holben, 1986). From the results in Figure 5, NDVI is more useful than DTSL in segmenting bare soil from vegetation, but DASL is more useful than NDVI in segmenting wet soil from dry soil. Neither technique is likely to be effective in segmenting snow and ice from mud. However, snow and bare ice may be distinguishable from mud (using the color bands of the multispectral camera) because they are brighter in color imagery than dry soil and mud is not. DASL may be useful in segmenting wet soil from soil in shadow, but it is probably not very useful in determining whether the soil in shadow is wet or dry.

4. MUD CUES FROM SWIR

Water strongly absorbs light in the NIR and SWIR wavelengths, suggesting that wet soil may also do so. Lobell and Asner (2002) acquired measurements of reflected shortwave radiation (400–2,500 nm) of four different soils at varying moisture levels in a laboratory setting using a spectrometer and a calibrated light source. They report that whereas reflectance for visible wavelength saturates at a SMC of 20%, reflectance for SWIR saturates at a much higher SMC (50%). They concluded that the SWIR region is more suitable for measuring SMC than NIR. The plot in Figure 6 (from Mouazen, Karoui, De Baerdemaeker, & Ramon, 2006) illustrates that increasing the SMC causes the largest change in reflectance in a narrow SWIR band near a wavelength of 1,450 nm. This suggests that passive SWIR may be useful in detecting mud. However, both the Lobell and Asner (2002) and Mouazen et al. (2006) experiments were performed in a laboratory setting where the lighting was controlled and the measurement unit was downward mounted in close proximity to the soil.

To assess the feasibility of using a forward-looking passive SWIR imaging sensor for mud detection, we evaluated outdoor SWIR imagery of wet and dry soil acquired during two data collections. The first data collection was performed during the PerceptOR program (Rankin, Bergh, Goldberg, Bellutta, Huerta, et al., 2005) using a Sensors Unlimited SU320M-1.7RT SWIR camera (under a

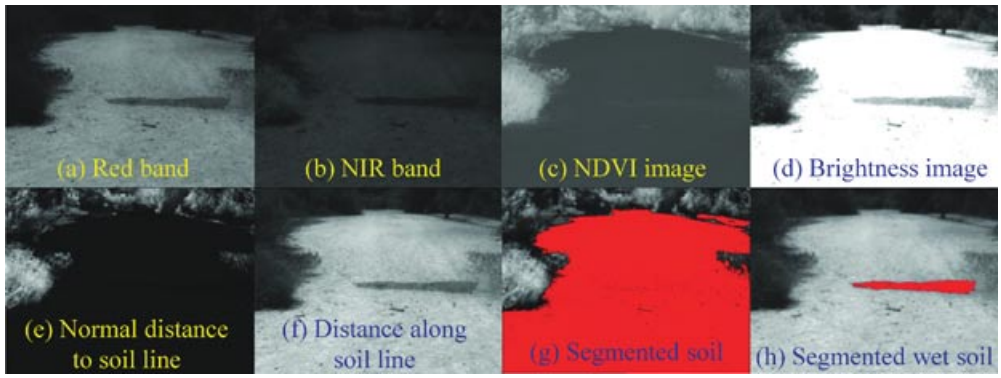

Figure 5. NIR and red bands of a multispectral camera can be useful in separating vegetation from soil and dry soil from wet soil.

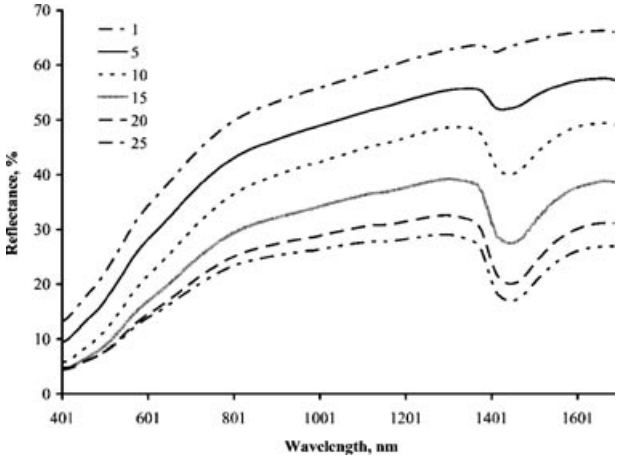

Figure 6. Average spectra recorded for 46 soil samples from a single field (from Mouazen et al., 2006). The curves correspond to SMC, having units of $\times 0.01$ kg of water per 1 kg of soil. Reprinted with permission from the *Soil Science Society of America Journal*.

short-term loan agreement with Uniforce Sales and Engineering, Milpitas, California). This camera contains a 320 × 240 InGaAs detector, spectrally sensitive from 900 to 1,700 nm. After acquiring visible and SWIR imagery of dry soil, a few buckets of water were poured on the soil and the scene was imaged again. The second data collection was performed using a Spiricon SP-1550IR SWIR camera. The SP-1550IR camera consists of a charge-coupled device (CCD) focal plane array coated with a phosphor that emits visible radiation when illuminated with infrared radiation in the 1,460–1,625-nm range. Visible and SWIR imagery was collected on naturally occurring bodies of mud and in a normally dry riverbed after several weeks of rain.

Sample visible and SWIR images from the two data collections are shown in Figures 7 and 8. When a scene is directly illuminated by the sun, dry soil, green vegetation, and rocks tend to be brighter in SWIR imagery than mud (Figure 7, upper left), but shadows and moving water tend to be darker than mud (Figure 7, lower left). Still water directly illuminated by the sun tends to be darker in SWIR imagery than mud where it reflects the sky but brighter than mud where it reflects objects such as rocks, buildings, or clouds (Figure 7, upper right). When the sun is occluded by clouds, wet soil is still darker than dry soil in SWIR imagery, but water can be brighter than wet soil if it is reflecting anything other than the sky, such as clouds (Figure 8).

For patches of soil with different SMC, SWIR intensity values decrease with increasing SMC, but the intensity differences can be visually barely noticeable and difficult to detect. Therefore, it is not likely that a forward-looking passive SWIR sensor can be reliably used to estimate SMC. In extremely wet conditions, SWIR imagery can be useful in identifying the wettest portions of terrain. We expect water-covered terrain to be relatively dark in SWIR imagery under most conditions. (One exception is where there is still water reflecting an object, such as the rock in the upper right image of Figure 7.) For example, the lower right image of Figure 7 illustrates how starkly moving water stands out in SWIR imagery.

If a SWIR camera is used for mud detection, one will need to disambiguate mud from other dark regions. Snow, ice, water, shadows, and dry vegetation can all cause dark regions in SWIR imagery. Snow and bare ice may be distinguishable from mud because they are brighter in color imagery than dry soil and mud is not. Water can be distinguished from mud by using color to detect sky reflections and stereo range data to detect terrain reflections (Rankin & Matthies, 2006). Color imagery can also be useful in

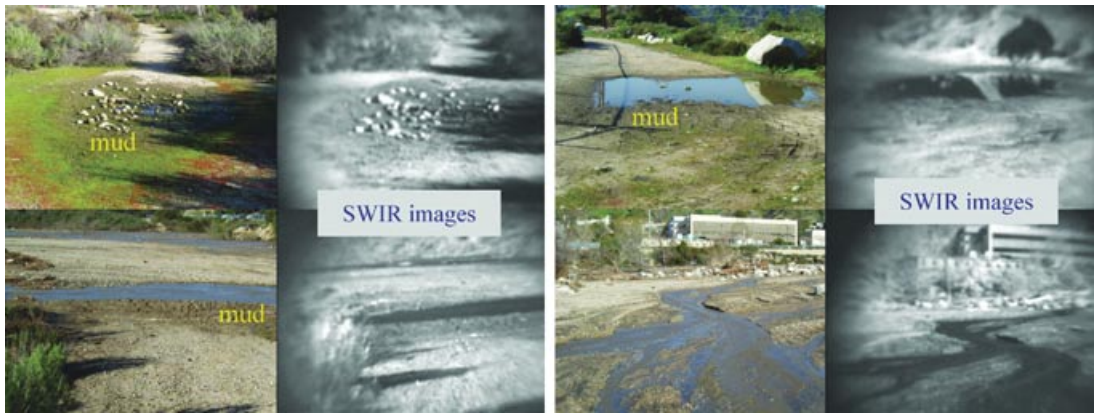

Figure 7. Visible and SWIR imagery of naturally occurring muddy conditions in the Los Angeles County Arroyo Seco on a sunny day. The SWIR images were acquired with a Spiricon SP-1550IR camera. A 1,100-nm low-pass filter was placed over the lens, causing the periphery of the SWIR images to appear dark.

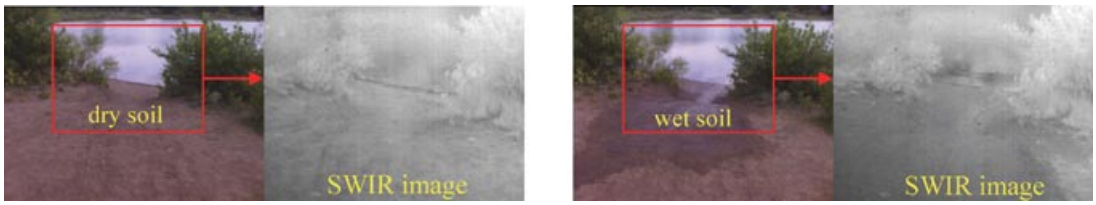

Figure 8. Visible and SWIR imagery of dry and wet soil, acquired from a UGV at Lake Chatfield, Colorado, on a partly cloudy day when the sun was occluded by a cloud. The red box overlaid on the visible images indicates the field of view of the SWIR camera (Sensors Unlimited SU320M-1.7RT).

disambiguating nonshadowed mud from shadows. Tall vegetation can be distinguished from mud by using stereo range data to separate ground clutter from the ground surface.

5. MUD CUES FROM THERMAL INFRARED

Factors that influence soil temperature include the angle to the sun, the SMC, whether the soil is in shadow, and the time of day. Soil color also influences temperature because darker colors tend to absorb and release energy more rapidly than lighter colors. Wet soil tends to be cooler than dry soil for a couple of reasons. First, evaporation helps to cool moist soil by dissipating heat. Second, the high heat capacity of water reduces the temperature change from the heat that is absorbed by the soil (Troeh & Thompson, 2005).

Two sensor classes lie within the thermal infrared portion of the spectrum: MWIR and LWIR. In general, MWIR sensors (constructed of InSb, HgCdTe, and PbSe) have a spectral sensitivity from 3 to 5 μm, and LWIR sensors (constructed of HgCdTe and microbolometers) have a spectral sensitivity from 7 to 14 μm. We recognize that there are subtle differences between cooled vs. uncooled and MWIR vs. LWIR sensors. But because mud is close to ambient temperature, and we do not expect extreme temperatures or a very wide range in temperatures on cross-country terrain, we expect the contrast between mud and surrounding terrain to be similar for high-end thermal infrared cameras, and thus group MWIR and LWIR sensors together as a single class.

To test the feasibility of using a thermal infrared imaging sensor for mud detection, we evaluated Cincinnati Electronics NC256 MWIR imagery collected during the PerceptOR program (Rankin et al., 2005) and performed an all-day data collection (6:20 a.m.–7:30 p.m.) on a body of mud with a Thermoteknix Systems Miricle 110KB LWIR camera, recording LWIR images and environmental conditions every 20 min. For the LWIR data collection, the temperature of the mud and surrounding dry soil was measured using a Fluke 52 Series II Thermometer, and air temperature and relative humidity were measured with a Springfield Instruments 91066. The MWIR camera has a 256 × 256 cooled InSb detector with a spectral sensitivity from 3.6 to 5 μm, and the LWIR camera has a 384 × 288 Alpha Silicon microbolometer detector with a spectral sensitivity from 7 to 14 μm. On the day of the LWIR data collection, there was a thick marine layer until 9:20 a.m., it was partially overcast until about 10:00 a.m., and then it was sunny for the remainder of the day.

Figure 9 shows a plot of the temperature of the dry soil, mud, and air over the entire day and sample LWIR

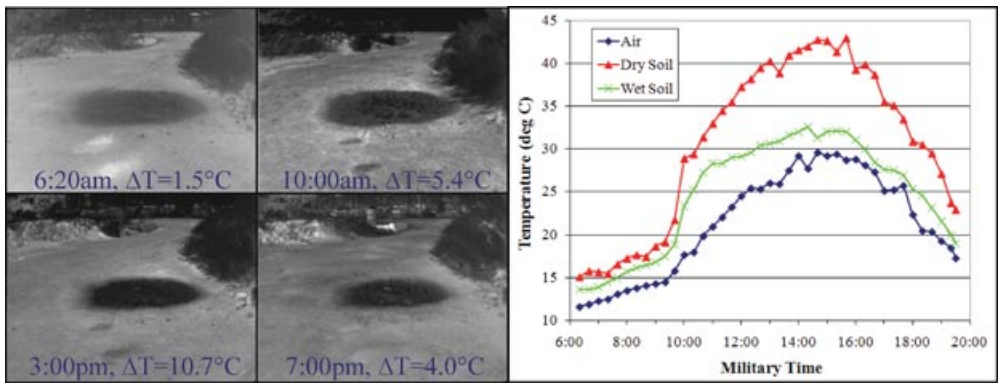

Figure 9. Under nominal weather conditions, mud has a strong signature in LWIR imagery throughout the day. ΔT is the difference in temperature between the mud and the surrounding dry soil. This is the same body of mud that is shown in the left image of Figure 1.

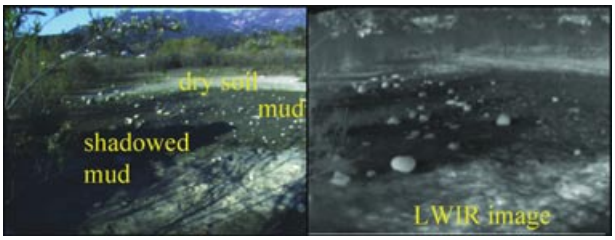

Figure 10. Under nominal weather conditions, mud is cooler than dry soil, and shadowed mud is cooler than nonshadowed mud during the daytime. This color and LWIR image is from the Los Angeles County Arroyo Seco.

images from 6:20 a.m., 10:00 a.m., 3:00 p.m., and 7:00 p.m. In the temperature plot, the mud was cooler than the soil during the entire day, even when there was heavy overcast. The temperature difference between the dry soil and mud started out low in the morning, rose to a peak in the midafternoon, and started to decline through the evening. The sample imagery confirms that under nominal weather conditions, wet soil is cooler than dry soil throughout the day in thermal infrared imagery. Even at the lowest temperature difference (1.5°C), there was still significant thermal contrast between the dry soil and the mud in the LWIR imagery.

However, not all the dark regions in thermal infrared imagery are candidate mud. Shadows, snow, ice, vegetation, and water can all cause dark regions in thermal infrared imagery. Snow and bare ice may be distinguishable from mud because they are brighter in color imagery than dry soil and mud is not. Tall vegetation can be distinguished from mud by using stereo range data to separate ground clutter from the ground surface. Water can be distinguished from mud by using color to detect sky reflections and stereo range data to detect terrain reflections (Rankin & Matthies, 2006). Figure 10 illustrates that under nominal weather conditions, mud in shadow is cooler than mud out of shadow during the daytime. As discussed in Section 2, shadows can be distinguished from nonshadowed mud by analyzing the hue component of color.

Thermal infrared imagery can provide a strong cue for mud during nominal weather conditions when nonmud dark regions are disambiguated with other sensors. In addition, a thermal infrared imaging sensor can be useful in detecting mud that is occluded by thin vegetation, such as pine needles and leaves (see the left frame of Figure 11). But under off-nominal conditions, such as after precipitation when the entire ground is damp, the usefulness of thermal infrared imagery for mud detection decreases. As illustrated with the MWIR image in the right frame of Figure 11, it is difficult to detect the muddiest portions of the trail from the rest of the wet trail in thermal infrared imagery.

6. MUD CUES FROM POLARIZATION

There are four fundamental properties of light: intensity, wavelength, coherence, and polarization. In the past, vision-based terrain classification methods have focused primarily on intensity and wavelength (color) properties. But with the recent emergence of polarization cameras, the components of polarization from light reflected off surfaces can also be exploited to classify terrain types. For example, Xie, Xiang, Pan, and Liu (2007) and Pandian (2008) have recently experimented with using a polarization camera to detect water.

Almost all naturally occurring outdoor light (scattered and reflected) is at least partially linearly polarized (Wolff, 2005). According to Rayleigh's law, skylight is nearly unpolarized close to the sun but becomes increasingly partially polarized as the angle to the sun increases. An overcast sky, however, is unpolarized. By placing a polarization filter in front of a sensor, the transmitted radiance of partial polarized light at each pixel will vary sinusoidally with a period of 180 deg in accordance with the filter orientation. Because a sinusoid can be uniquely characterized by three points, three images with different polarization filter orientations are required to fully characterize linear polarized light. If filter orientations of 0, 45, and 90 deg are chosen, the linear polarization parameters can be calculated at each pixel by Eqs. (1)–(3), where I_0, I_{45}, and I_{90} are pixel intensity values for each filter orientation. The degree of linear polarization

Figure 11. A thermal infrared imager can be useful in detecting mud occluded by pine needles or leaves (left frame). However, when the entire ground is wet after precipitation, it would be difficult to use thermal infrared imagery to detect the muddiest portions of the terrain (right frame). These images are from Ft. Polk.

(DOLP) at each pixel is a value between 0 (completely unpolarized light) and 1 (completely linear polarized light):

$$\text{Phase} \quad \theta = \left(\frac{1}{2}\right)\tan^{-1}\left[\frac{I_0 - 2I_{45} + I_{90}}{I_{90} - I_0}\right] + 90, \qquad (1)$$

$$\text{if}\,(I_{90} < I_0)\ \{\text{if}\,(I_{45} < I_0)\ \theta = \theta + 90; \quad \text{else}\ \theta = \theta - 90;\},$$

$$\text{Intensity} \quad I = I_0 + I_{90}, \qquad (2)$$

$$\text{DOLP} = \frac{I_{90} - I_0}{(I_{90} + I_0)\cos(2\theta)}. \qquad (3)$$

To calculate a simplified polarization measure called *polarization contrast*, only two images of a scene are required, as long as the polarization filter orientations differ by 90 deg. If one of the filter orientations is aligned with the orientation of the linearly polarized component in the input light, i.e., phase angle $\theta = 0$, then polarization contrast equals DOLP. Otherwise, polarization contrast provides a lower bound for DOLP (Pandian, 2008). Because water and mud appear to be horizontally polarized, if filter orientation angles of 0 deg (*parallel*) and 90 deg (*crossed*) are chosen, polarization contrast can be used to estimate the DOLP on water and mud. As shown in Eq. (4), the polarization contrast at each pixel can be calculated by dividing the absolute value of the difference between the parallel and crossed intensity values by the sum of the parallel and crossed intensity values:

$$\text{Polarization contrast} = \frac{\|I_{90} - I_0\|}{I_{90} + I_0}. \qquad (4)$$

Regions of a natural terrain scene that have a significantly higher DOLP than surrounding terrain can be a potential cue for water. However, the DOLP of reflections from water bodies is a function of the incidence angle—hence look-ahead distance. Moreover, it will also be affected by the polarization of the light incident on the water, which is dependent on sky conditions, sun position, and viewing geometry, as well as the polarization of light upwelling from within the water body. Therefore, there are conditions in which the DOLP on water will not be significantly higher than on surrounding terrain. As an example, Xie et al. (2007) found that water reflecting nearby vegetation had a DOLP almost the same as that of the surrounding terrain. Perovich (1998) acquired outdoor DOLP measurements at a wavelength of 550 nm on dry snow, wet snow, smooth ice, rough ice, and very shallow water (6 cm deep) on sunny days, varying the azimuth angle (between the sensor and sun) and the sensor zenith angle. The DOLP was very low (<5%) for azimuth angles greater than 45 deg for all samples.

Sun, Hong, and Qiao (2009) used a multiband polarized camera to measure the DOLP of yellow–brown soil (from Hefei, Anhui, China) at nine different levels of SMC in a laboratory setting, at wavelengths of 443, 555, and 665 nm. A beam of unpolarized light from a 400-W tungsten–halogen lamp was directed at the soil samples. The light source was mounted 1.5 m from the soil sample at an incidence angle of 40 deg. The angle between the light source axis and the camera optical axis was varied from 30 to 100 deg, and the SMC was varied from 0% to 43.9% (mass water/mass soil). The measured DOLP was inversely proportional to the wavelength. All of the DOLP measurements at the SMC level of 21.58% exceeded the corresponding dry soil DOLP measurements, except for one, which was equal. But at the other soil moisture levels, the results were mixed. Some wet soil DOLP measurements were lower than the corresponding dry soil DOLP measurements, and some were higher. In general, DOLP increased with increasing phase angle up to a SMC of approximately 30%. For all of the DOLP measurements, the light source, camera optical axis, and soil sample surface normal were oriented in a single incident plane.

To further assess whether polarization can be useful in detecting mud, we performed outdoor experiments on sunny and overcast days, on bodies of mud without limits on the sun incidence angle or requiring an incident plane, with a sensor sensitive to the entire visible spectrum. Several daytime data collections were performed with a SAMBA polarization camera and a SALSA linear Stokes polarization camera, both obtained under short-term loan agreements with Bossa Nova Technologies (Venice, California). The SAMBA polarization camera contains a single CCD sensor and automatically switches between two polarization filter orientations (0 and 90 deg), acquiring parallel and crossed images in rapid succession. The time that elapses between acquiring the parallel and crossed images is roughly equivalent to the user-specified exposure time, where the minimum allowable exposure time is approximately 8.3 ms. The SAMBA camera outputs parallel and crossed polarization images. The corresponding polarization contrast images are then generated in software. The SALSA camera uses an optical active polarization modulator to acquire four polarization images at filter orientations of −45, 0, 45, and 90 deg. These images, acquired successively at video frame rate, are output by the camera, and the linear polarization parameters (phase angle, intensity, DOLP) are calculated for each pixel in software.

In the first data collection, SAMBA polarization imagery of a single body of mud was acquired every 20 min for more than 7 h from a stationary position with the sensor facing northeast. The data collection started at 6:20 a.m. and ended at 1:40 p.m. To provide power to the data collection hardware, we used a high mobility multiwheeled vehicle (HMMWV) that contained a propane generator. A full-day data collection was planned, but the propane generator failed prior to the 2:00 p.m. collection. A circular region of soil having a radius of approximately 2 m was periodically watered for 3 days prior to the data collection to ensure a mud consistency. There was a thick marine layer

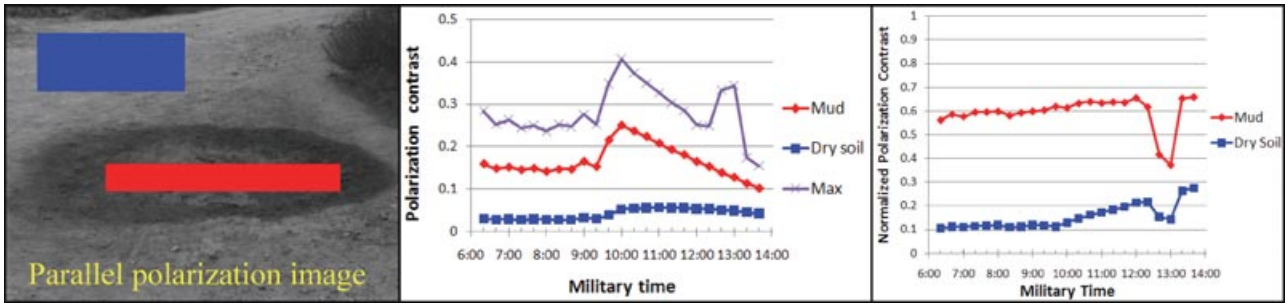

Figure 12. The average polarization contrast for the sample red mud region was larger than the average polarization contrast for the sample blue dry soil region over the entire 7-h, 20-min data collection from a stationary camera position. Polarization contrast was normalized by dividing by the maximum polarization contrast over an image.

at the beginning of the data collection, but by 9:20 a.m., the sun started to peek through it, and by 10:00 a.m., it had completely evaporated. Figure 12 shows polarization contrast and normalized polarization contrast plots for sample mud and dry soil regions. The polarization contrast on the mud was higher than on the surrounding dry soil in all the samples. Figure 13 shows the parallel and crossed polarization images, the resultant polarization contrast images, and segmented mud images for three intermediate times during the data collection. The same parameters were used to segment the mud for all cases.

The polarization contrast on water can change based on sky conditions, the sun position, and the sensor orientation. But the polarization contrast on mud appears to be consistently higher than the polarization contrast on surrounding dry soil, regardless of those conditions. This is illustrated in two examples from a sunny day. In both examples, water was poured on a body of mud, leaving a rim of wet soil around the boundary. In Figure 14, the body of water was imaged from three directions (facing southwest, southeast, and northeast), each separated by approximately 90 deg. Note that the polarization contrast on the wet soil around the rim of the water bodies is consistently higher than on the surrounding dry soil, even when the polarization contrast on the water is not. Unfortunately, when transferring the imagery from the data collection computer

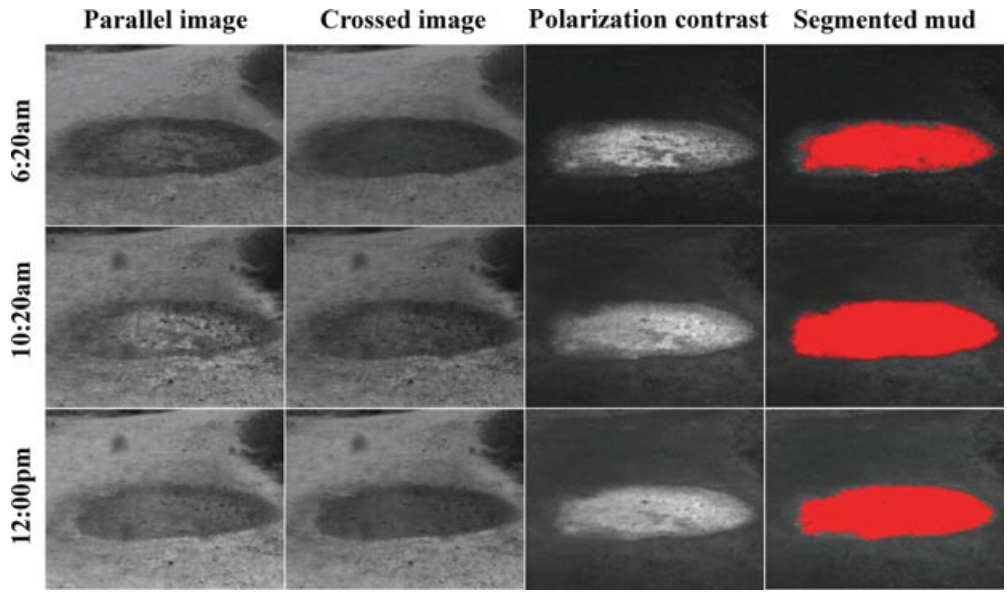

Figure 13. Segmenting mud using SAMBA polarization imagery at different times of the day from a stationary camera position. The sensor zenith angle was ~104 deg for the entire data collection. At 6:20 a.m., the sky was overcast. At 10:20 a.m., the sun was out, the solar zenith angle was 35.2 deg, and the azimuth angle was 38.9 deg. At noon, the solar zenith angle was 16.6 deg and the azimuth angle was 135.1 deg.

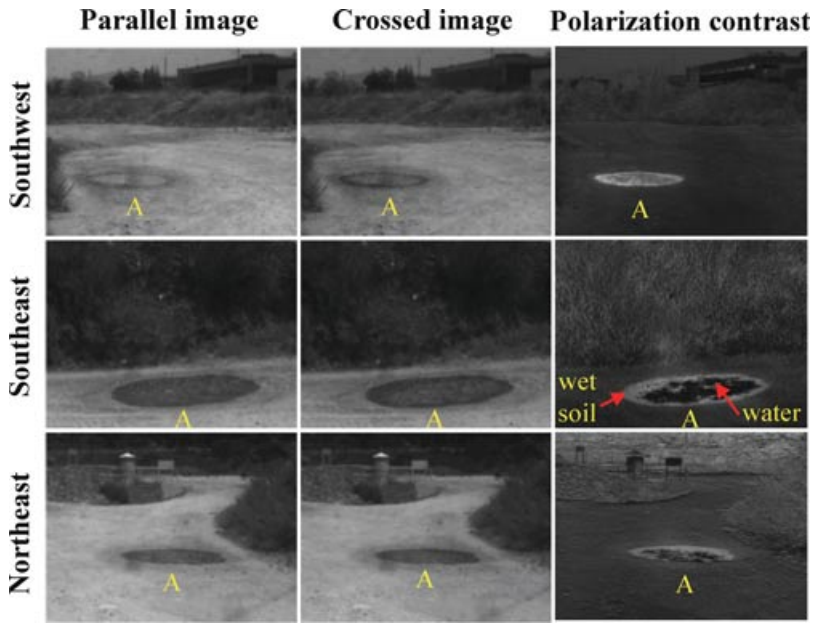

Figure 14. A body of mud (A) with water poured on it, imaged on a sunny day from three directions (facing southwest, southeast, and northeast) with a SAMBA polarization camera. The images for each heading were acquired a few minutes apart. The polarization contrast on the wet soil around the rim is consistently higher than that on the surrounding dry soil, even when the polarization contrast on the water is not.

to an archive, the time for each image was changed from the capture time to the copy time. Therefore, we are unable to specify the solar zenith angle and the azimuth angle for the images in Figures 14 and 15. The example in Figure 15 illustrates that the polarization signature on mud occurs at close and far range and on tire tracks in mud.

In a second data collection, a stereo pair of color cameras and a SALSA polarization camera were mounted to the

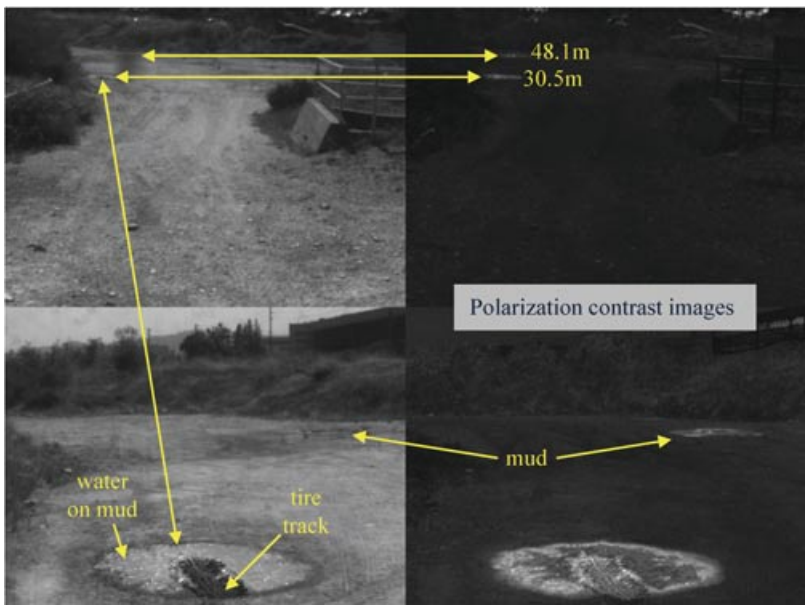

Figure 15. A SAMBA parallel and polarization contrast image of bodies of mud at far and close range. The close mud body in this example contains a tire track. In the top row images, the ranges to the two bodies of mud are 30.5 and 48.1 m.

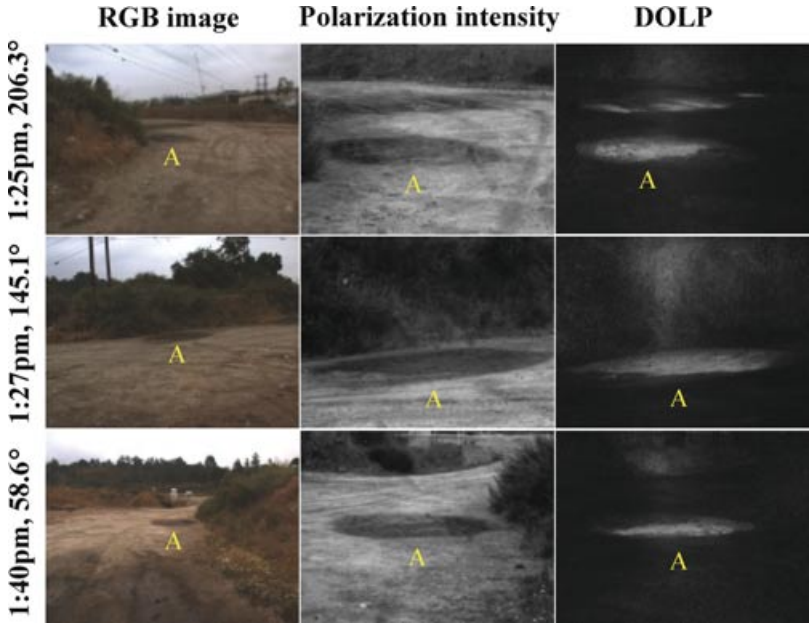

Figure 16. A body of mud (A) imaged on an overcast day from three directions (facing southwest, southeast, and northeast) with a stereo pair of color cameras and SALSA polarization camera. The DOLP on mud during an overcast day is consistently higher than that on surrounding dry soil, independent of sensor orientation. The horizontal fields of view of the color and polarization cameras are 55.8 and 20 deg, respectively.

hood of the HMMWV and a body of mud was imaged from three different directions (facing southwest, southeast, and northeast). This data collection took place from 1:25 p.m. to 1:40 p.m. on an overcast day. As illustrated in Figure 16, in all three cases, the DOLP on the mud was consistently higher than that on the surrounding dry soil. The DOLP on some types of vegetation can be higher than on dry soil. An example of this can be seen in the middle row of Figure 16. In Section 7, we will discuss a method for restricting the search for mud to the load-bearing surface, eliminating false detection on vegetation. There is one case in which we have observed a weak polarization signature on wet soil. As illustrated in Figure 17, the DOLP on wet soil in shadow can be very similar to the DOLP on dry soil in shadow. In addition, water and mud cannot be distinguished solely using DOLP. However, water can be distinguished from mud by using color to detect sky reflections and stereo range data to detect terrain reflections (Rankin & Matthies, 2006).

7. MUD CUES FROM STEREO

Thus far, we have discussed appearance-based cues for mud that are detectable over portions of the visible through thermal infrared spectrum. However, there are also geometric cues for mud that could be exploited with a passive ranging method such as stereo vision. For example, we expect mud to occur only on load-bearing surfaces of natural terrain. By geometrically detecting a structure that lies above the load-bearing surface and flagging it as ground clutter, we can reduce the space required to be searched with appearance-based methods and as a result, reduce the false-positive mud detection rate.

To test the feasibility of using stereo vision to detect and remove ground clutter, we performed a stereo data collection on a scene in the Los Angeles County Arroyo Seco that contained a dirt trail lined with ground clutter. A stereo pair of Hitachi HV-F31 3-CCD color cameras was mounted to the hood of a HMMWV with a camera separation

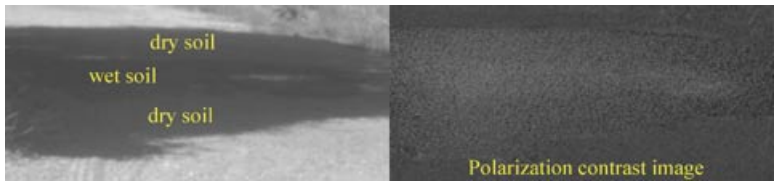

Figure 17. A SALSA intensity and DOLP image of wet soil in shadow on a sunny day. The solar zenith angle was 37.4 deg, and the azimuth angle was 115.7 deg. The DOLP of wet soil in shadow is similar to the DOLP of the dry soil in shadow.

distance of 50 cm. The HMMWV contains a Honeywell Modular Azimuth Positioning System (MAPS) inertial navigation system (INS) and a NovAtel RT-20 global positioning system (GPS) that receives differential corrections from a base station GPS receiver via a radio modem. A navigation solution is generated at 25 Hz by an external Kalman filter that integrates INS and GPS data.

The HMMWV was manually driven down the trail while logging stereo images and navigation data to disk. Images were captured and logged at a resolution of 1,024 × 768 pixels and processed offline at a resolution of 512 × 384 pixels using JPL RCTA stereo correlation software (Rankin, Huertas, & Matthies, 2009). For each stereo pair of images, a stereo range image is generated in which each pixel contains three-dimensional (3D) coordinates in a vehicle coordinate system (which is aligned with the north and east directions). The coordinates of each pixel in the stereo range image can be transformed into global coordinates for building a Cartesian grid–based world map. In addition, a stereo range image is pixel registered with the corresponding rectified left color image.

Ground clutter detection and removal can be performed on a frame-by-frame basis using stereo range images. As an alternative, the stereo range images can be merged into a single composite world map that records elevation statistics for each cell. Then ground clutter detection and removal could be performed on the world map. Figure 18 shows an example of ground clutter detection and removal performed on a 40-cm-resolution world map generated from a single stereo pair of color images. Ground clutter detection and removal is performed by thresholding the standard deviation of the terrain elevation, the local tilt of the terrain (estimated with a least squares plane fit), and the plane-fit residual.

The local tilt of the terrain is calculated over 1.2 × 1.2 m terrain patches (3 × 3 grid cells) using the minimum elevation measurement within each cell. For each new stereo range image, local tilt is recalculated only for each 1.2 × 1.2 m terrain patch that has new data. The stereo elevation overlay in Figure 18 shows the z coordinate for each pixel in the latest stereo range image, color coded for elevation. The other overlays contain map elevation standard deviation, tilt, plane-fit residual, and load-bearing surface data, transformed from map space into image space. In the elevation and plane-fit overlays, red corresponds to low values, blue corresponds to high values, and the colors in between correspond to an intermediate value. The stereo point cloud after ground clutter removal extends out approximately 50 m.

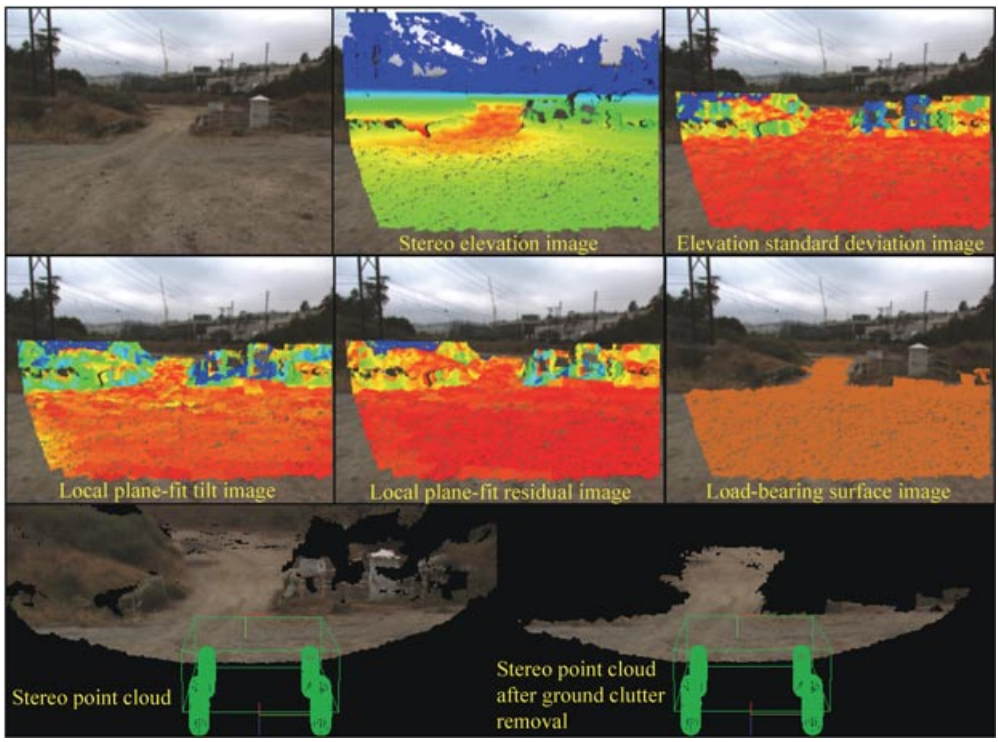

Figure 18. Mud occurs only on load-bearing surfaces of natural terrain. Ground clutter detection and removal is performed in a composite world map by thresholding the standard deviation of the terrain elevation, the local tilt of the terrain (estimated with a least squares plane fit), and the plane-fit residual. In the elevation and plane-fit overlays, red corresponds to low values, blue corresponds to high values, and the colors in between correspond to an intermediate value. The images in the bottom row contain a stereo point cloud before and after ground clutter removal.

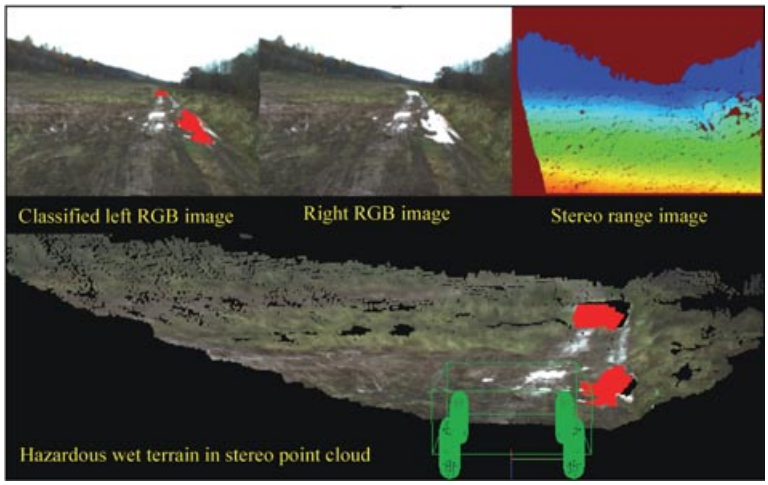

Figure 19. When the entire ground is wet, for example, after several days of rain, it makes little sense to perform mud detection. Mud is everywhere. Under these conditions, color stereo imagery can be used to detect, localize, and avoid the wettest regions. Here, only sky reflection regions with a large surface area are classified as nontraversable.

Not every region of the load-bearing surface is a candidate for mud, however. Water tends to run down the load-bearing surface and collect in areas where there is a local concavity. Then over many days, as the water body evaporates out, a muddy surface may remain. We are currently experimenting with using stereo range data to isolate the portions of the load-bearing surface that contain a local concavity.

In Figure 3, we illustrate using color to detect wet terrain that is oversaturated. After several days of rain, the entire ground may be muddy. Some UGVs may be operated under such conditions. For example, during the RCTA capstone experiment at Ft. Indiantown Gap in October 2009, autonomous navigation tests were performed following several days of heavy rain. The scene in Figure 19 is of a muddy field where some of the autonomous tests occurred. When mud is everywhere, it makes little sense to perform mud detection. One strategy for operating on wet terrain is to simply avoid the wettest terrain. The combination of color imagery and stereo range data can be used to detect, localize, and avoid the wettest terrain in areas that are out in the open. In Figure 19, only sky reflection regions with a large surface area are classified as nontraversable.

8. MUD LOCALIZATION IN A TERRAIN MAP

Mud detected by a UGV's perception system should be placed within the vehicle-level world map that the UGV uses to plan safe paths. In this section, we illustrate the process with a multisensor-based mud detection solution. A SALSA polarization camera was used to classify mud, and a stereo pair of Hitachi HV-F31 color cameras was used to localize detected mud and reject false-positive mud detection on ground clutter. The first row of Figure 20 shows

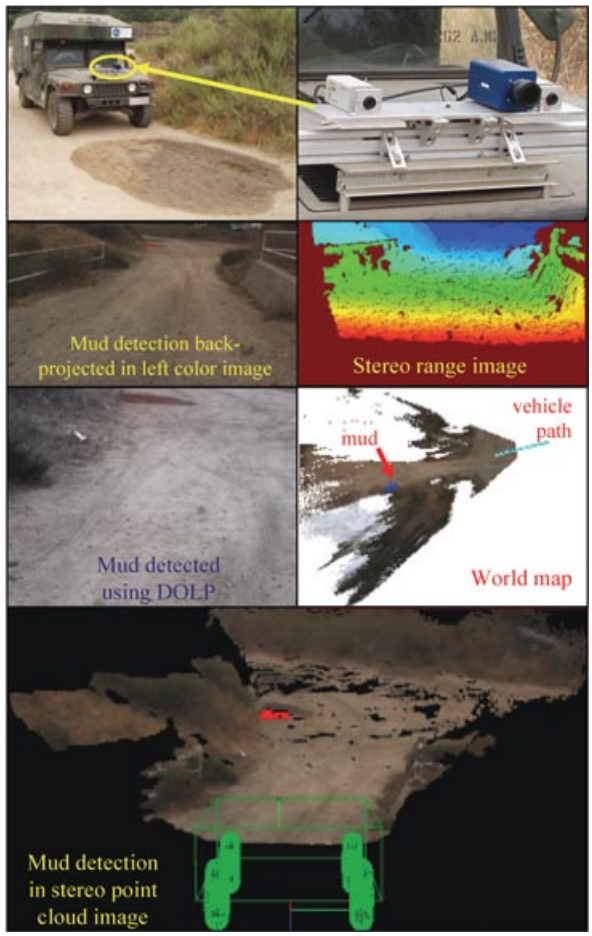

Figure 20. Classifying and localizing mud in a world map using a SALSA polarization camera and a stereo pair of color cameras.

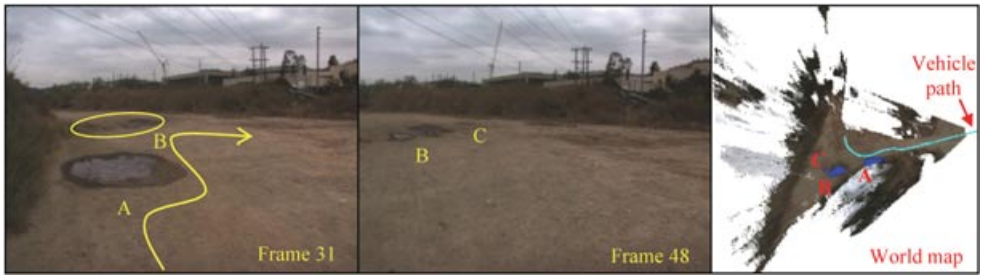

Figure 21. Detected mud localized in a world map (in blue) for the full 66-frame sequence.

the sensors mounted to the hood of a HMMWV with the color cameras having a separation distance of 50 cm. All three sensors were calibrated within the vehicle coordinate system. Because the SALSA polarization camera does not acquire polarization imagery for its four filter positions at the same time, imagery from the SALSA polarization camera needs to be acquired with the vehicle stationary. The HMMWV was manually driven toward the body of mud shown in the upper left image, with the vehicle stopping approximately every meter to acquire and log polarization and stereo imagery to disk.

A mud detection algorithm was implemented that thresholds DOLP and backprojects polarization pixels that have a high DOLP into the rectified left color image (which is registered with the stereo range image). The images in rows 2–4 of Figure 20 are from frame 12 during the drive, illustrating mud detection from a range of 27 m. The last row of Figure 20 shows the mud detection results in the stereo point cloud. As illustrated by the bird's-eye view of the world map, mud detection, terrain elevation, and average terrain color are accumulated over time in a north-oriented world map containing 40-cm resolution cells. Dark blue indicates the location of detected mud, cyan indicates the vehicle path, and white indicates cells that have no data. The other colors are the average color of the terrain within that cell. As we expect mud to occur only on the load-bearing surface, stereo vision was used to isolate load-bearing surface pixels from the other pixels corresponding to ground clutter.

Figure 21 shows the final world map for the full 66-frame sequence and left color images from two intermediate frames. All of the mud in the scene was correctly classified and localized in the world map with no false-positive mud detection. The first detection of mud body A was in the first frame of the sequence at a range of 30.5 m. A portion of mud body B was also detected in the first frame at a range of 48.1 m. Mud body B is actually a cluster of closely spaced small bodies of mud. At far range, however, it appears as a single body in the polarization imagery. The world map contains cumulative detections from all the frames in the sequence, which accounts for mud body B being oversized in the world map. Map fading of cells within the polarization camera's field of view could be used to improve the shape of the detected mud in the world map. For this particular scene, vegetation with a high DOLP was not placed within the world map because those pixels are a part of the ground clutter. We are currently implementing color-based segmentation, which will improve the robustness of this detector.

9. CONCLUSIONS

A military UGV stuck in a body of mud during a mission may need to be sacrificed or rescued, both unattractive options. Thus, robust mud detection is a critical perception requirement for UGV cross-country autonomous navigation. A passive mud detection solution is desirable to meet future combat system requirements. Several characteristics of mud may be detectable with an appropriate passive sensor. Under the Demo III, PerceptOR, and RCTA programs, JPL performed daytime data collections on wet and dry soil using a variety of passive imaging sensors that spans much of the visible through thermal infrared portion of the electromagnetic spectrum. These include color stereo, multispectral (visible plus NIR), SWIR, MWIR, LWIR, and polarization. In this paper, we have characterized the strengths and weaknesses of each passive sensor type for detecting mud during the daytime from a UGV under ideal conditions (isolated wet soil surrounded by dry soil during nominal weather). Table II lists the strengths and weaknesses for each sensor type.

A camera sensitive to the visible spectrum can be useful in segmenting mud surrounded by dry soil (because mud is darker than dry soil), detecting patches of water on oversaturated soil, and disambiguating unshadowed mud from shadows and snow, ice, and water from mud. In addition, a stereo pair of color cameras can be used to segment the load-bearing surface and localize mud in a world map. However, color is probably not very useful in determining whether the terrain in a shadow is mud or in distinguishing the muddiest portion of terrain when the entire ground is wet, except where there are small patches of water reflecting the sky.

A camera that outputs visible and NIR spectral bands can be useful in segmenting soil from vegetation (based on NDVI) and mud from dry soil (based on DASL). However, modeling of the soil line for different types of soil is required. Both NDVI and DASL are likely to be ineffective in

Table II. Strengths and weaknesses of passive sensors evaluated for mud detection.

Stereo	Color	Red/NIR	SWIR	Thermal infrared	Polarization
			Strengths		
−Can be used to localize detected mud in a world map −Can segment load-bearing surface based on geometry	−Segment mud from dry soil based on color −Disambiguate unshadowed mud from shadows (based on blue tinge), snow, bare ice, and water −Detect sky reflection in watery mud	−Segment soil from vegetation based on NDVI −Segment mud from dry soil based on the soil line	−SWIR reflectance saturates at higher SMC than visible wavelengths (mud becomes progressively darker as SMC increases) −Segment wettest portion of terrain in extremely wet conditions	−Segment mud from dry soil based on thermal signature (mud is cooler than dry soil the entire day during nominal weather) −Segment mud occluded by thin layer of vegetation (e.g., pine needles)	−Segment mud based on DOLP −Polarization signature on mud is strong independent of sun position, sky conditions, and UGV sensor orientation
			Weaknesses		
−Other cues are needed for robust mud detection	−Cannot determine whether terrain in shadow is mud or dry soil −Poor detection if entire ground is wet with no watery patches	−Modeling of soil line required for different soil types −Poor disambiguation of mud from ice (more data are needed)	−Snow, ice, water, shadows, and ice all cause dark regions in SWIR imagery −Extensive modeling required to estimate SMC	−Shadows, snow, ice, water are also cooler than dry soil −Extensive modeling required for off-nominal weather conditions	−Poor detection of mud in shadow (more data are needed)

segmenting snow and ice from mud. However, snow and bare ice may be distinguishable from mud using the color bands because they are brighter in color imagery than dry soil and mud is not. DASL may be useful in segmenting wet soil from soil in shadow, but it is probably not very useful in determining whether the soil in shadow is wet or dry.

In SWIR imagery, wet soil progressively becomes darker as the SMC increases. In fact, SWIR reflectance saturates at a higher SMC than visible and NIR wavelengths, making SWIR an attractive band for estimating SMC. However, extensive modeling is likely required to elicit accurate soil moisture levels from SWIR imagery. Shadows, snow, ice, and water can all cause dark regions in SWIR imagery, but they may be distinguishable from mud if a stereo pair of color cameras is used in combination with a SWIR camera. In extremely wet conditions, SWIR imagery can be useful in identifying the wettest portions of terrain.

A thermal infrared camera can be useful in segmenting mud surrounded by dry soil because mud is cooler than dry soil the entire day during nominal weather. A thermal signature is apparent even when the mud is occluded by a thin layer of vegetation, such as pine needles. However, extensive modeling is required to handle off-nominal conditions. Shadows, snow, ice, and water are also cooler than dry soil, but they may be distinguishable from mud if a stereo pair of color cameras is used in combination with a thermal infrared camera. Under conditions in which the entire ground is wet, it would be difficult to detect the muddiest portions of the terrain from the rest of the wet terrain in thermal infrared imagery.

A polarization camera can be very useful in segmenting mud surrounded by dry soil because the DOLP on mud is consistently higher than on surrounding dry soil, regardless of sky conditions, the sun position, and the sensor orientation. There is one case, however, in which we have observed a weak polarization signature on wet soil: the DOLP on wet soil in shadow can be very similar to the DOLP of dry soil in shadow. In addition, water and mud cannot be distinguished solely using DOLP. Smooth ice can have a high DOLP when the azimuth angle is low, but the DOLP on dry and wet snow is fairly low, regardless of azimuth angle (Perovich, 1998). Water and ice may be distinguishable from mud if a stereo pair of color cameras is used in combination with a polarization camera.

None of the passive sensors that we evaluated are fully capable of disambiguating mud from all other common terrain types. As a result, a multisensor approach to mud detection is desired. The combination of color, stereo, and

polarization appears to be well suited for robust daytime mud detection (under ideal conditions) and false alarm rejection. A mud detection algorithm was implemented that thresholds DOLP and backprojects polarization pixels that have a high DOLP into the rectified left color image, which is registered with a stereo range image. A ground clutter detection algorithm is used to limit mud detection to the perceived load-bearing surface. Because the SAMBA and SALSA polarization cameras that we have experimented with sequentially capture polarization imagery, they are not well suited for high-speed UGVs. We have procured a Flux Data FD-1665 polarization camera, which is capable of acquiring three simultaneous polarization images of a scene at 20 frames per second. The FD-1665 contains a single lens and aperture, a beam splitter, three point Gray Research color (Bayer pattern) CCD cameras, and a polarization filter on each CCD. Additional near-term work includes developing a second mud detector that fuses cues from color, stereo, and polarization. More work is needed to characterize the usability of the sensors evaluated in this paper to detect mud under nonideal conditions.

ACKNOWLEDGMENTS

The research described in this paper was carried out by JPL, California Institute of Technology, and was sponsored by the ARL RCTA program through an agreement with the National Aeronautics and Space Administration. Reference herein to any specific commercial product, process, or service by trademark, manufacturer, or otherwise does not constitute or imply its endorsement by the U.S. Government or JPL, California Institute of Technology.

REFERENCES

Alshikaili, T.Y. (2007). Non-contact measurement of soil moisture content using thermal infrared sensor and weather variables. Master's thesis, University of Saskatchewan, Saskatoon, Saskatchewan.

Angelova, A., Matthies, L., Helmick, D., & Perona, P. (2007). Learning and prediction of slip from visual information. Journal of Field Robotics, 24(3), 205–231.

Archer, F., Shutko, A.M., Coleman, T.L., Haldin, A., Novichikhin, E., & Sidorov, I. (2004, September). Introduction, overview, and status of the Microwave Autonomous Copter System (MACS). In Proceedings of the IEEE International Symposium on Geoscience and Remote Sensing, Anchorage, AK (pp. 3574–3576).

Archer, F., Shutko, A., Coleman, T.L., Haldin, A., Sidorov, I., & Novichiknin, E. (2006, July). Microwave remote sensing of soil moisture from a rover and robotic aerial platform: The Alabama experiments. In Proceedings of the 18th World Congress on Soil Science, Philadelphia, PA.

Dubois, P.C., & van Zyl Engman, J. (1995). Measuring soil moisture with imaging radars. IEEE Transactions on Geoscience and Remote Sensing, 33(4), 915–926.

DuPont, E.M., Collins, E.G., Coyle, E.J., & Roberts, R.G. (2008). Terrain classification using vibration sensors: Theory and methods. In E. Gaines & L. Peskov (Eds.), New research on mobile robotics. Hauppauge, NY: Nova Science Publisher, Inc.

Hamrita, T.K., Tollner, E.W., & Schafer, R.L. (2000). Toward fulfilling the robotic farming vision: Advances in sensors and controllers for agricultural applications. IEEE Transactions on Industry Applications, 36(4), 1026–1032.

Holben, B.N. (1986). Characteristics of maximum-value composite images from temporal AVHRR data. International Journal of Remote Sensing, 7(11), 1417–1434.

Lobell, D.B., & Asner, G.P. (2002). Moisture effects on soil reflectance. Soil Science Society of America Journal, 66, 722–727.

Matthies, L., Bellutta, P., & McHenry, M. (2003, April). Detecting water hazards for autonomous off-road navigation. Proceedings of SPIE, 5083, 231–242.

Mills, M.E. (2007, October). Challenges to the acceptance and proliferation of tactical UGVs. RUSI Defence Systems, 10(2), 28–30.

Mouazen, A.M., Karoui, R., De Baerdemaeker, J., & Ramon, H. (2006). Characterization of soil water content using measured visible and near infrared spectra. Soil Science Society of America Journal, 70, 1295–1302.

Ollis, M. & Stentz, A. (1997, September). Vision-based perception for an autonomous harvester. In Proceedings of IEEE/RSJ International Conference on Intelligent Robots and Systems, Grenoble, France (pp. 1838–1844).

O'Neill, P., Chauhan, N., & Jackson, T. (1996). Use of active and passive microwave remote sensing for soil moisture estimation through corn. International Journal of Remote Sensing, 17(10), 1851–1865.

Pandian, A. (2008). Robot navigation using stereo vision and polarization imaging. Master's thesis, Institut Universitaire de Technologie IUT Le Creusot, Université de Bourgogne.

Perovich, D.E. (1998). Observations of the polarization of light reflected from sea ice. Journal of Geophysical Research, 103(C3), 5563–5575.

Persson, M. (2005). Estimating surface soil moisture from soil color using image analysis. Vadose Zone Journal, 4, 1119–1122.

Powers, M. & Davis, C. (2009, April). Optical signatures for autonomous mobility. Proceedings of SPIE, 7324, 73240U-11.

Rankin, A., Bergh, C., Goldberg, S., Bellutta, P., Huertas, A., & Matthies, L. (2005, March). Passive perception system for day/night autonomous off-road navigation. Proceedings of SPIE, 5804, 343–358.

Rankin, A., Huertas, A., & Matthies, L. (2009, April). Stereo vision based terrain mapping for off-road autonomous navigation. Proceedings of SPIE, 733210.

Rankin, A., & Matthies, L. (2006, November). Daytime water detection and localization for unmanned vehicle autonomous navigation. In Proceedings of the 25th Army Science Conference, Orlando, FL.

Rankin, A., Matthies, L., & Huertas, A. (2004, November). Daytime water detection by fusing multiple cues for autonomous off-road navigation. In Proceedings of the 25th Army Science Conference, Orlando, FL.

Sudduth, K.A., Hummel, J.W., & Birrell, S.J. (1997). Sensors for site-specific management. In F. Pierce and E. Sadler (Eds.), The state of site-specific management for agriculture (pp. 183–210). Madison, WI: ASA-CSSA-SSSA.

Sun, X., Hong, J., & Qiao, Y. (2009, February). Measurements of multi-angle polarization properties of the water-bearing yellow brown soil using multi-band polarimetric imagery in the laboratory. In Proceedings of SPIE, Beijing, China (vol. 7160).

Troeh, F.R., & Thompson, L.M. (2005). Soils and soil fertility. Boston: Blackwell Publishing.

Twomey, S.A., Bohren, C.F., & Mergenthaler, J.L. (1986). Reflectances and albedo differences between wet and dry surfaces. Applied Optics 25, 431–437.

Wells, B. (2007, December). Detection and manipulation of shadows in an image or series of images. U.S. Patent #7305127.

Wetzel, P.J., Atlas, D., & Woodward, R. (1984). Determining soil moisture from geosynchronous satellite infrared data: A feasibility study. Journal of Climate and Applied Meteorology, 23, 375–391.

Whalley, W.R. & Stafford, J.V. (1992). Real-time sensing of soil water content from mobile machinery: Options for sensor design. Computers and Electronics in Agriculture, 7(4), 269–284.

Wigneron, J.P., Schmugge, T., Chanzy, A., & Kerr, C.Y. (1998). Use of passive remote sensing to monitor soil moisture. Agronomia, 18, 27–43.

Wolff, L.B. (2005). Applications of polarization camera technology. IEEE Expert: Intelligent Systems and Their Application, 10(5), 30–38.

Xie, B., Xiang, Z., Pan, H., & Liu, J. (2007). Polarization-based water hazard detection for autonomous off-road navigation. In Proceedings of the IEEE/RSJ International Conference on Intelligent Robots and Systems, San Diego, CA (pp. 3186–3190).

Zeng, Y., Feng, Z., & Xiang, N. (2004, September). Assessment of soil moisture using Landsat ETM+ Temperature/Vegetation index in semiarid environment. In Proceedings of the IEEE International Symposium on Geoscience and Remote Sensing, Anchorage, AK (pp. 4306–4309).